Journal of Advanced Ceramics
2019, **8**(3): 399–407
https://doi.org/10.1007/s40145-019-0322-8
ISSN 2226-4108
CN 10-1154/TQ

Research Article

Mechanical and dielectric properties of porous and wave-transparent Si_3N_4–Si_3N_4 composite ceramics fabricated by 3D printing combined with chemical vapor infiltration

Zanlin CHENG, Fang YE*, Yongsheng LIU, Tianlu QIAO, Jianping LI, Hailong QIN, Laifei CHENG, Litong ZHANG

Science and Technology on Thermostructure Composite Materials Laboratory, Northwestern Polytechnical University, Xi'an 710072, China

Received: October 19, 2018; Revised: January 27, 2019; Accepted: March 2, 2019

Abstract: Porous Si_3N_4–Si_3N_4 composite ceramics were fabricated by 3D printing combined with low-pressure chemical vapor infiltration (CVI). This technique could effectively improve the designability of porous Si_3N_4 ceramics and optimize the mechanical and dielectric properties. The effects of process parameters including the deposition time and heat treatment on the microstructure and properties of porous Si_3N_4–Si_3N_4 composite ceramics were studied. The study highlights following: When CVI processing time was increased from 0 to 12 h, the porosity decreased from 68.65% to 26.07% and the density increased from 0.99 to 2.02 g/cm^3. At the same time, the dielectric constant gradually increased from 1.72 to 3.60; however, the dielectric loss always remained less than 0.01, indicating the excellent electromagnetic (EM) wave-transparent performance of porous Si_3N_4–Si_3N_4 composite ceramics. The maximum flexural strength of 47±2 MPa was achieved when the deposition time attained 6 h. After heat treatment, the porosity increased from 26.07% to 36.02% and the dielectric constant got a slight increase from 3.60 to 3.70 with the dielectric loss still maintaining lower than 0.01. It has been demonstrated that the porous Si_3N_4–Si_3N_4 composite ceramics are a promising structural and EM wave-transparent material suitable for high temperature service.

Keywords: porous Si_3N_4 ceramics; Si_3N_4–Si_3N_4 composite ceramics; mechanical property; electromagnetic (EM) wave transparent performance; 3D printing; chemical vapor infiltration (CVI)

1 Introduction

The radome and antenna windows, which are used on carrier rockets, airships, missiles, and return satellites, are made of excellent electromagnetic (EM) wave-transparent materials. The critical nature of aerospace and military technology requires excellent mechanical and dielectric properties, adequate thermal shock resistance, thermal resistance, and erosion resistance [1, 2]. Some metallic oxides offer high mechanical strength, excellent hardness, and erosion resistance. However, the dielectric constant is relatively high, and they usually exhibit a strong temperature dependence such

* Corresponding author.
E-mail: yefang511@nwpu.edu.cn

as Al_2O_3 [3]. Some nitrides can act as the EM wave-transparent material because of the low dielectric constant, dielectric loss, high melting point, and low coefficient of thermal expansion. However, the low mechanical properties and rain erosion resistance limit the applications in advanced fields such as BN [3]. Besides, Si_3N_4 ceramics are also a potential EM wave-transparent material for radome applications, which possess excellent mechanical properties but relatively high dielectric constant (5.6 in 8–10 GHz, compared with 3.3 of fused silica) [4,5]. The dielectric constant of Si_3N_4 ceramics can be reduced by increasing the porosity of ceramics. The porous Si_3N_4 ceramics with 40%–55% of porosity exhibit the low dielectric constant of 2.7–3.3 [3,6].

The porous Si_3N_4 ceramic preforms can be prepared by a number of shaping methods, such as die pressing process, cold isostatic pressing process, and gel-casting process [3]. However, these shaping methods involve complicated processing and poor machinability. Three-dimensional (3D) printing is a novel technique based on the principle of ink-jet printing, which can rapidly produce complex 3D structures, especially for prototype purposes [7,8]. It is demonstrated that 3D printing possesses the capability of fabricating various functional materials including ceramics, metals, and polymers [8,9]. Hence, 3D printing can be used to realize the near-net-shape forming of porous Si_3N_4 ceramic preforms [10–13]. Then, a densification technique is needed to adjust and control the microstructure of porous Si_3N_4 ceramics in order to optimize the mechanical and dielectric properties. Chemical vapor infiltration (CVI) technique is considered as an effective method to fabricate Si_3N_4 matrix with expected and controlled composition in the porous preforms. During CVI, the gas diffusion mechanism depends on the pore size of preforms and the mean free path of gas molecules [3,14,15]. If the open pores of preforms are appropriately large, Si_3N_4 matrix can be deposited inside the preforms. Therefore, CVI technique is an effective way to achieve the proper density and porosity of Si_3N_4 ceramics.

In this study, porous Si_3N_4–Si_3N_4 composite ceramics were prepared by 3D printing technique combined with CVI technique. The mechanical and dielectric properties of composite ceramics as a function of deposition time were explored, and the effects of heat treatment on the microstructure and properties were also investigated.

2 Experimental

The slurries were prepared by mixing 85 wt% of Si_3N_4 powders (D = 50 μm; Hefei Morco New Materials Technology Co., Ltd., China), 10 wt% of dextrin (Tianjin Dingshengxin Chemical Industry Co., Ltd., China), and 5 wt% of Lu_2O_3 (Beijing HWRK Chemical Co., Ltd., China) in deionized water, followed by ball milling in a barrel ball mill with agate balls at a speed of 100 rpm for 24 h. After being dried at 120 ℃ and sieved through an 80-mesh (180 μm) screen, the uniformly mixed powders had been prepared for 3D printing as described in the previous work [16]. The fabrication of porous Si_3N_4 preform was performed by 3D printer (Spectrum Z510, Z Corporation, USA). The mixed powders were put into the feed platform and were swept into the build platform via a slider. The slider moved at a speed of approximately 300 mm/s. Then the print head sprayed the binder to bond the powders. When the 3D printer printed each layer, the thickness of the powders was set to 0.05 mm. The specimens with the sizes of 22.8 mm × 10.16 mm × 2.86 mm and 40 mm × 5 mm × 3 mm were fabricated to evaluate the dielectric and mechanical properties, respectively. The incorporated organic binder was eliminated through oxidization in the air at 800 ℃ for 24 h. The specimens were wrapped in BN powders and placed in a graphite crucible, and the sintering was carried out by using a hot pressing furnace at 1800 ℃ and 0.3 MPa in N_2 atmosphere for 2 h. Finally, the porous Si_3N_4 ceramics were obtained.

Then these samples were put into a CVD/CVI furnace to infiltrate Si_3N_4 ceramics using silicon tetrachloride ($SiCl_4$ ≥ 99.99%) and ammonia (NH_3 ≥ 99.99%) as gas resources at 1000 ℃. Hydrogen (H_2 ≥ 99.99%) was used as the carrier gas of $SiCl_4$ and dilution gas, while argon (Ar ≥ 99.9%) was the dilution gas. The experiment was carried out for different durations including 0, 3, 6, 9, and 12 h, and the as-prepared Si_3N_4–Si_3N_4 composite ceramics were according designated as S0, S1, S2, S3, and S4, respectively. S4 was heat treated at 1500 ℃ in N_2 atmosphere for 2 h.

The morphology was observed by field-emission scanning electron microscope (FESEM, S-4700, Hitachi, Japan) at the acceleration voltage of 30 kV. The specimens were coated with a thin layer of gold to avoid the charging effect during scanning electron microsccpy (SEM) observations due to the low electrical conductivity. The crystal structure and phase

composition were assessed by X-ray diffraction (XRD; D8-Advance, Bruker, Karlsruhe, Germany), which collected the data from 10 ° to 90° of 2θ. An energy dispersion spectrometer (EDS) was used to analyze the elemental composition of the specimens. The density and open porosity were measured according to the Archimedes method and Eqs. (1) and (2):

$$P = \frac{m_w - m_d}{m_w - m_f} \quad (1)$$

$$\rho = \frac{m_d \times d}{m_w - m_f} \quad (2)$$

where P represents the open porosity (vol%); ρ corresponds to the density (g/cm^3); m_d refers to the mass of dry specimens; m_w represents the mass of the specimens with water-filled pores; m_f refers to the mass of the specimens immersed in water; and d corresponds to the density of water.

The flexural strength of specimens was measured by three-point bend test according to ASTM-C1341-00 standard and was conducted on an electronic universal testing machine (CMT4304, SANS, China) at the span of supporting points of 30 mm. The flexural strength and modulus were calculated using Eqs. (3) and (4):

$$\sigma_f = \frac{3PL}{2bh^2} \quad (3)$$

$$E_f = \frac{L^3 \times \Delta P}{4bh^3 \times \Delta f} \quad (4)$$

where σ_f refers to the flexural strength (Mpa); P represents the largest load when specimens were broken; L corresponds to the span of supporting points; b refers to the rectangular width of the pressure surface; h represents the thickness of specimens; E_f refers to the modulus; ΔP corresponds to the change in load during the elastic stage and Δf corresponds to the deflection increment.

The vector network analyzer (VNA, MS4644A, Anritsu, Kanagawa, Japan) was used to measure the dielectric properties in the frequency range of 8.2–12.4 GHz including the relative complex permittivity of specimens ($\varepsilon = \varepsilon' - j\varepsilon''$, ε' represents the real part and ε'' refers to the imaginary part).

3 Results and discussion

3. 1 Microstructural characterization

Figure 1 presents the macro morphologies of 3D-printed porous Si_3N_4 ceramic substrates before binder removal, after binder removal and sintering, which were referred as S0-0, S0-1, and S0-2, respectively. The 3D-printed porous Si_3N_4 ceramics are near-net-shaped. The process of binder removal made the substrate shrunk with the linear shrinkage ratio of 2%. After sintering, the shrinkage ratio increased to 22%. By EDS analysis results shown in Table 1, compared with S0-0, the C content of S0-1 has shown a significant decrease from 12.72 to 0.08. The XRD patterns of specimens are shown in Fig. 2. The binder removal temperature at 800 ℃ was not high enough (1400 ℃) for the transformation from α-Si_3N_4 to β-Si_3N_4. Hence, the 3D-printed porous Si_3N_4 ceramics after binder removal still composed of α-Si_3N_4 with a little amount of $Lu_2Si_2O_7$, indicating the unchanged crystal structure. After sintering at 1800 ℃, the crystal structure of ceramics changed from α-Si_3N_4 to β-Si_3N_4.

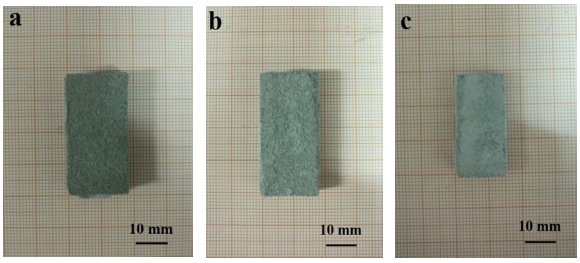

Fig. 1 Macro morphologies of 3D-printed porous Si_3N_4 ceramic substrates: (a) S0-0, (b) S0-1, and (c) S0-2.

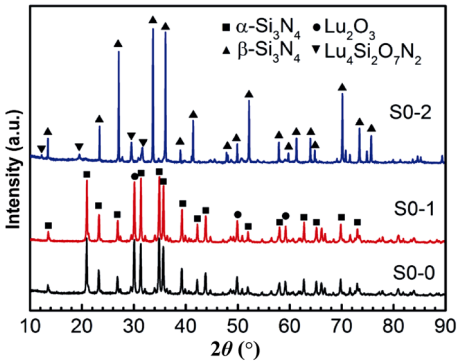

Fig. 2 XRD patterns of porous Si_3N_4 ceramic substrates.

Table 1 Elemental composition of 3D-printed porous Si_3N_4 ceramic substrates

Sample	EDS (at%)			
	Si	C	N	Lu
S0-0	33.10	12.72	54.05	0.13
S0-1	47.12	0.08	52.43	0.37
S0-2	43.56	0.34	55.35	0.75

3. 2 Effects of deposition time

Table 2 shows the variation of weight, porosity, and density of porous Si_3N_4–Si_3N_4 composite ceramics as a function of deposition time from 0 to 12 h. With the increase of deposition time, the weight of ceramics significantly increased. After CVI of 12 h, the porosity decreased from 68.65% to 26.07%, while the density increased from 0.99 to 2.02 g/cm^3. It is obvious that the pores in the porous Si_3N_4 ceramic substrates were filled by Si_3N_4 matrix via CVI process. Figure 3 shows the microstructure and morphologies of porous Si_3N_4–Si_3N_4 composite ceramics as a function of deposition time. The small-sized and rod-like β-Si_3N_4 grains were wrapped by the amorphous, cauliflower-like, continuous, and dense Si_3N_4 matrix via CVI process. Figure 3(a) presents SEM image of porous Si_3N_4 ceramic substrate after CVI for 0 h. The porous microstructure is clearly visible, and the pores are evenly distributed in the substrate and the average diameter is about 4 μm. The β-Si_3N_4 grains are mutually lapped and cross-linked with adjacent grains. The axial length of β-Si_3N_4 columnar grain is about 3 μm, while the columnar radius is about 1 μm. With the CVI duration time increasing, The internal pores of Si_3N_4–Si_3N_4 composite ceramics were gradually filled with CVI-Si_3N_4, and the material gradually became dense. Figure 4 shows XRD of porous Si_3N_4–Si_3N_4 composite ceramics with different deposition time. The diffraction peaks of β-Si_3N_4 and $Lu_4Si_2O_7N_2$ were easily detected because of the high crystallization degree of porous Si_3N_4 ceramic substrates. Considering that Si_3N_4 matrix via CVI process in this study is amorphous, the degree of amorphousness gradually increased with the increase of deposition time.

Figure 5 shows the dielectric properties in 8.2–12.4 GHz of porous Si_3N_4–Si_3N_4 composite ceramics with different CVI duration time. As deposition time increased, the pores in ceramic substrates were filled by CVI-Si_3N_4 matrix. The dielectric constant of CVI-Si_3N_4 matrix is lower than that of highly crystalline β-Si_3N_4 but higher than that of air. So the real part of permittivity increases with the CVI duration time increasing as shown in Fig. 5(a). After CVI of 6 h, the real part of permittivity increased from 1.72 (before deposition) to 2.26, which is still lower than the dielectric constant (3.23) of porous Si_3N_4 ceramics with 57% of porosity fabricated by pressureless sintering, indicating the excellent EM wave-transparent performance of as-prepared composite ceramics. The imaginary part of permittivity fluctuated around 0, and

Table 2 Weight, density, porosity, and flexural strength of porous Si_3N_4–Si_3N_4 composite ceramics

Deposition time (h)	Weight increment (compared with substrate) (%)	Density (g/cm^3)	Porosity (%)	Average flexural strength (MPa)
0	—	0.99	68.65	5 ± 0.6
3	88.83	1.28	53.83	21.7 ± 2.8
6	113.91	1.42	48.13	47 ± 2.6
9	148.43	1.75	34.56	42 ± 2.8
12	162.27	2.02	26.07	35 ± 3.8

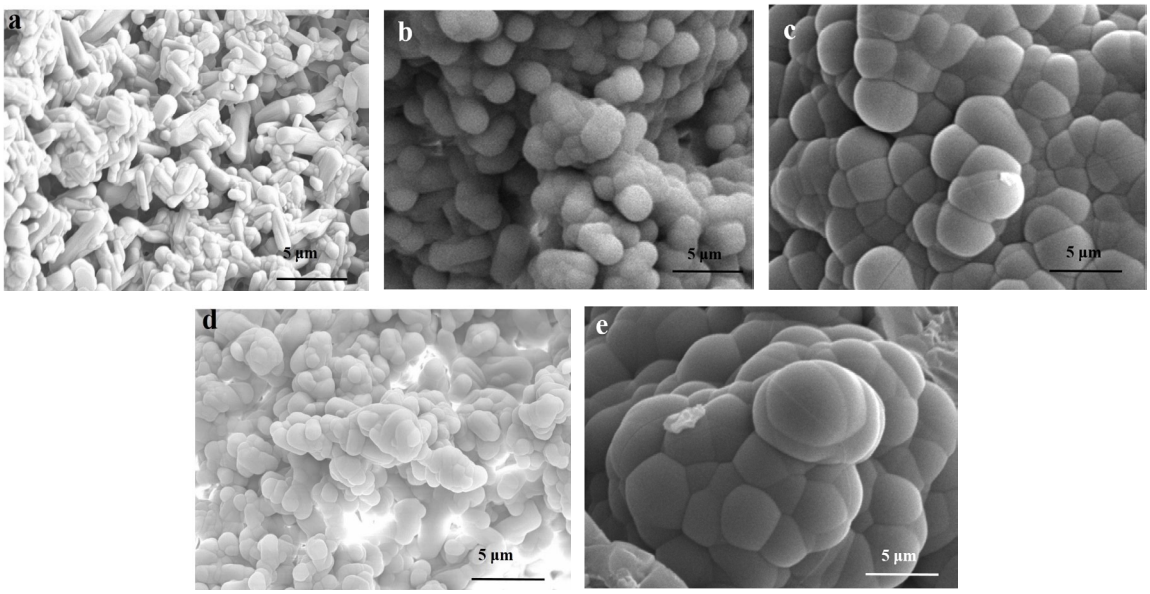

Fig. 3 Micrographs of porous Si_3N_4–Si_3N_4 composite ceramics as a function of deposition time: (a) 0, (b) 3, (c) 6, (d) 9, and (e)12 h.

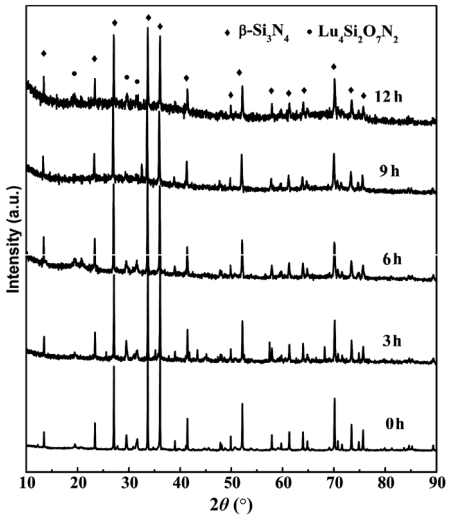

Fig. 4 XRD patterns of porous Si_3N_4–Si_3N_4 composite ceramics as a function of deposition time.

the fluctuation range was less than 0.003 in the studied frequency range (Fig. 5(b)). The amount of grains per unit volume decreases on account of the relatively high porosity, and the interfacial area of porous Si_3N_4 ceramics in this study also decreases, resulting in the reduction of electron scattering and EM wave energy loss. Despite a slight increase in the real part of permittivity with deposition time, the dielectric loss still remained low in the range of –0.01–0.01 (Fig. 5(c)).

The mechanical properties of porous Si_3N_4–Si_3N_4 composite ceramics as a function of deposition time are presented in Table 2. With the increase of deposition time, the density of composite ceramics gradually increased, while the porosity decreased. The flexural strength has first shown an obvious increase, followed by a slight decrease. After CVI of 6 h, the average flexural strength of 47±2.6 MPa was attained. The average flexural strength then decreased to 35± 3.8 MPa when the deposition time was extended to 12 h. The flexural strength of porous ceramics mainly depends on the porosity and size of pores. The maximum flexural strength can be attained by a uniform distribution of pores and the appropriate content of matrix. With the further increase of deposition time, the pore distribution gradient inevitably aggravated due to the bottleneck effect of CVI process. Besides, the further increased content of amorphous Si_3N_4 matrix can be responsible for the strength degradation.

Figure 6 shows the fracture morphologies of porous Si_3N_4–Si_3N_4 composite ceramics with different CVI duration time. When the deposition time was no more than 6 h, the porosity decreased and the bonding among particles were strengthened, resulting in the remarkably enhanced flexural strength as the deposition time increased. At this time, the debond and pull out of β-Si_3N_4 grains wrapped in Si_3N_4 matrix can be observed from the fracture morphologies images as shown in Fig. 7(a), indicating the effective carrying capacity of β-Si_3N_4 frameworks. However, when the deposition time was more than 6 h, the content of amorphous Si_3N_4 matrix further increased, leading to the predictable increase in the thermal stress caused by thermal mismatch in the composite ceramics. Many cracks generated accordingly, which made the strength of β-Si_3N_4 frameworks degraded. At this time, the fracture of ceramics was even without the debond and pull out of β-Si_3N_4 grains observed as shown in Fig. 7(b).

Mostly, the flexural strength of ceramics mainly depends on the bonding among ceramic particles. The particles reinforced materials should have strong interfacial bonding between matrix and particles for

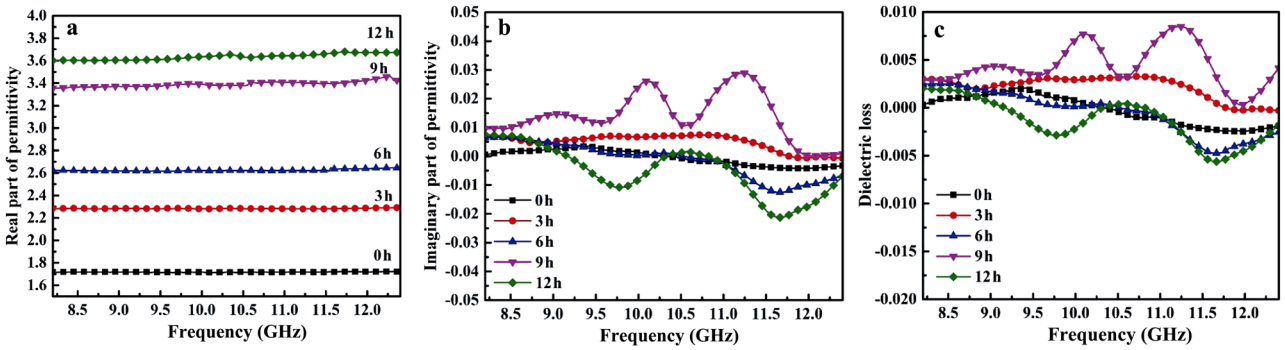

Fig. 5 Dielectric properties in 8.2–12.4 GHz of porous Si_3N_4–Si_3N_4 composite ceramics as a function of deposition time: (a) the real part of permittivity, (b) the imaginary part of permittivity, and (c) dielectric loss.

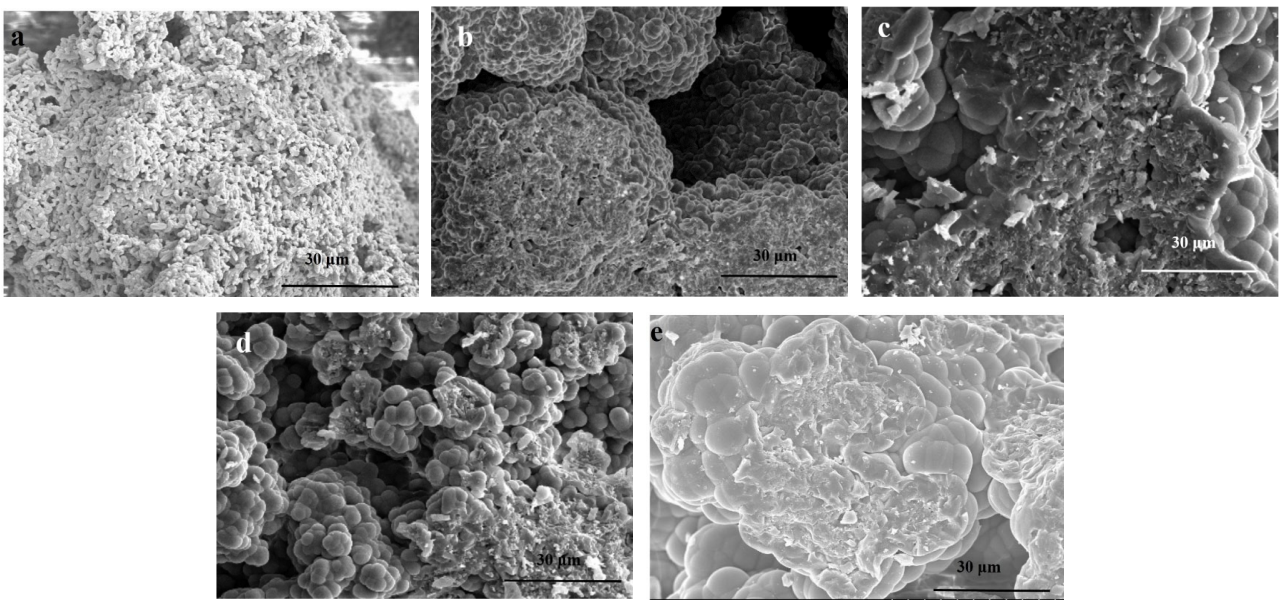

Fig. 6 Fracture morphologies of porous Si_3N_4–Si_3N_4 composite ceramics as a function of deposition time: (a) 0, (b) 3, (c) 6, (d) 9, and (e)12 h.

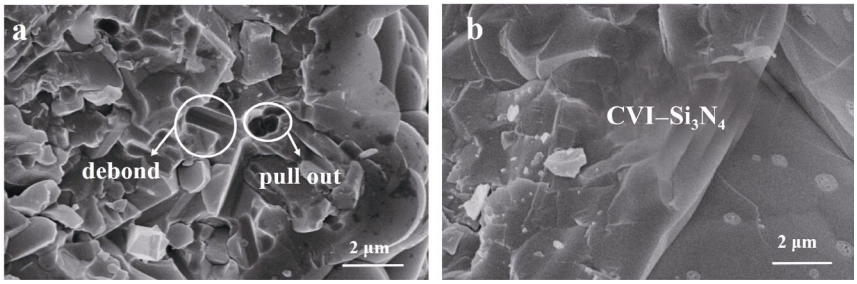

Fig. 7 High-resolution fracture morphologies of porous Si_3N_4–Si_3N_4 composite ceramics as a function of deposition time: (a) 3 and (b) 12 h.

the uniform and effective distribution of applied load. At the same time, the pores among ceramic particles should be relatively small and uniformly distributed to disperse the applied stress and avoid the cracking failure effectively. In this study, porous Si_3N_4 ceramics exhibited the loose and porous microstructure even after the deposition of Si_3N_4 matrix and the interfacial bonding between β-Si_3N_4 grains and the amorphous Si_3N_4 matrix was not strong. It was hard for β-Si_3N_4 grains to develop the maximum load-bearing capacity, and the flexural strength of porous Si_3N_4–Si_3N_4 composite ceramics attained the medium level (about 50 MPa), consequently.

3. 3 Effects of heat treatment

Generally, high-temperature treatment (heat treatment) can affect the microstructure, phase composition, and properties such as mechanical and functional properties of ceramic materials. Therefore, it is necessary to investigate the impacts of heat treatment on the microstructural evolution, mechanical and EM wave-transparent properties, variations of porous Si_3N_4–Si_3N_4 composite ceramics, considering their potential application at high temperature.

Table 3 compares the weight, density, and porosity of composite ceramics (S4) before and after heat treatment. It is found that the mass loss attained about 4.85%, the density decreased from 2.02 to 1.99 g/cm^3, and the porosity increased from 26.07% to 36.02% due to the volume shrinkage, phase decomposition, and crystallization of ceramics during heat treatment process. Figure 8 shows that the degree of crystallization increased and the amorphous Si_3N_4 matrix via CVI process was transformed into α-Si_3N_4 after heat treatment along with the volume shrinkage. Figure 9 presents the surface morphologies of composite ceramics (S4) before and after heat treatment. The smooth, dense, and amorphous convex hull microstructure of Si_3N_4

matrix can be clearly observed before heat treatment (Figs. 9(a) and 9(b)). However, the micro-cracks with a width of about 1 μm appeared in Si_3N_4 matrix after heat treatment (Fig. 9(c)) and many fine particles corresponding to the crystallization of amorphous phase formed in the convex hull (Fig. 9(d)). It is worth mentioning that the transformation of amorphous Si_3N_4 matrix into α-Si_3N_4 changed the atomic configuration from the loose state to the close packing state, leading to the generation of micro-cracks. In addition, the difference in coefficient of thermal expansion between α-Si_3N_4 and β-Si_3N_4 caused thermal mismatch as a result of the production of micro-cracks.

Table 3 Weight, density, porosity, and flexural strength of porous Si_3N_4–Si_3N_4 composite ceramics (S4) before and after heat treatment

Specimen	Weight increment (%)	Density (g/cm^3)	Porosity (%)	Average flexural strength (MPa)
Before HT	—	2.02	26.07	35 ± 3.8
After HT	–4.85	1.99	36.02	23.3 ± 2.3

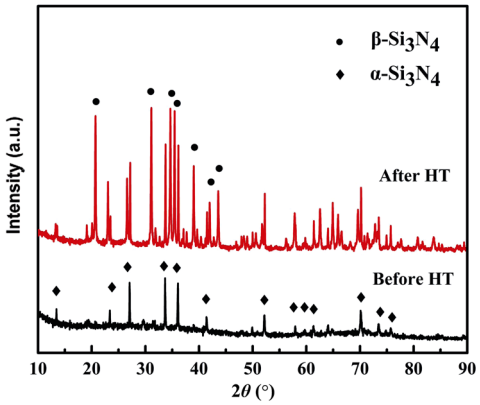

Fig. 8 XRD patterns of porous Si_3N_4–Si_3N_4 composite ceramics (S4) before and after heat treatment. "HT" represents "heat treatment".

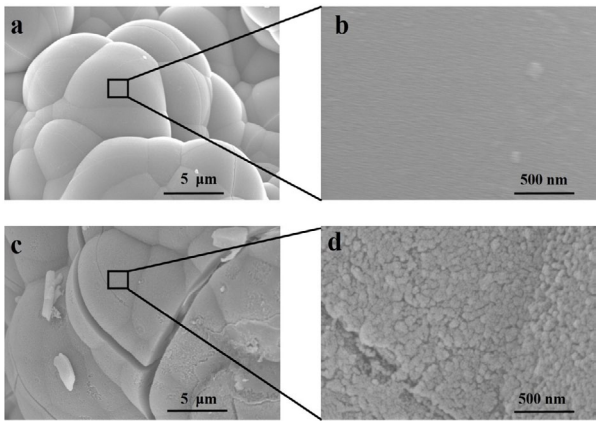

Fig. 9 Micrographs of porous Si_3N_4–Si_3N_4 composite ceramics (S4): (a, b) before heat treatment and (c, d) after heat treatment.

The dielectric properties of porous Si_3N_4–Si_3N_4 composite ceramics (S4) before and after heat treatment are presented in Fig. 10. It is found that the real part of permittivity of ceramics slightly increased from 3.60 to 3.70 after heat treatment, considering the higher permittivity of α-Si_3N_4 than that of amorphous Si_3N_4 (Fig. 10(a)). The imaginary part of permittivity of ceramics remained around 0 after heat treatment (Fig. 10(b)). Accordingly, the dielectric loss stayed around 0 and the vibration range was less than 10^{-2} (Fig. 10(c)). This shows that although the CVI-Si_3N_4 matrix changes from amorphous to α-Si_3N_4 after 1500 ℃ heat treatment, porous Si_3N_4–Si_3N_4 composite ceramics

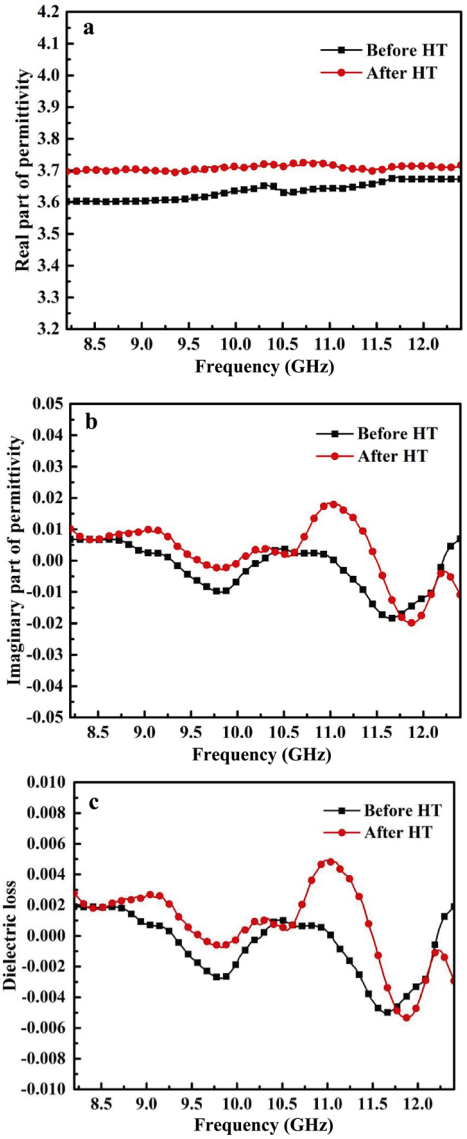

Fig. 10 Dielectric properties in 8.2–12.4 GHz of porous Si_3N_4–Si_3N_4 composite ceramics (S4) before and after heat treatment: (a) the real part of permittivity, (b) the imaginary part of permittivity, and (c) dielectric loss.

can maintain good EM wave-transparent ability. On the other hand, the study has shown that the temperature coefficients of permittivity and dielectric loss of Si_3N_4 keep around 10^{-4} $(℃)^{-1}$, which means that Si_3N_4 ceramics exhibit excellent thermo-stability of dielectric response with the increase of temperature [17]. Therefore, the porous Si_3N_4–Si_3N_4 composite ceramics in this paper are expected to have excellent EM wave-transparent ability even at 1500 ℃ considering the dielectric properties and wave-transparent performance of α-Si_3N_4 crystallized in the composite ceramics annealed at 1500 ℃.

Table 3 compares the flexural strength of composite ceramics (S4) before and after heat treatment. The average flexural strength decreased from 35±3.8 to 23.3±2.3 MPa. With the increased porosity, the bonding between particles in ceramics was impaired. Figure 11 shows the fracture morphologies of composite ceramics (S4) before and after heat treatment. The micro-cracks appeared in Si_3N_4 matrix after heat treatment, induced by the crystal structure transformation of Si_3N_4 phase and the thermal mismatch. It is inferred that the increased porosity and the occurrence of micro-cracks were mainly responsible for the deceased flexural strength.

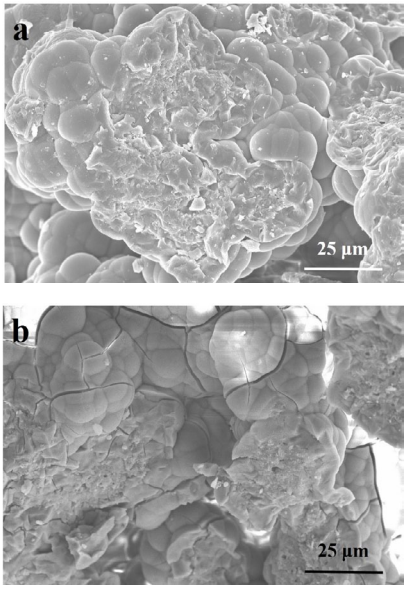

Fig. 11 Fracture morphologies of porous Si_3N_4–Si_3N_4 composite ceramics (S4): (a) before heat treatment and (b) after heat treatment.

4 Conclusions

In this study, porous Si_3N_4–Si_3N_4 composite ceramics were prepared by 3D printing combined with CVI technique. This preparation method can improve the designability of porous Si_3N_4 ceramics effectively and optimize the mechanical and dielectric properties. The effects of deposition time and heat treatment on the microstructure and properties of composite ceramics have been explored. The main conclusions of this study are given below:

(1) The crystal structure of 3D-printed porous Si_3N_4 ceramic substrates changed from α-Si_3N_4 to β-Si_3N_4 after sintering, and the columnar β-Si_3N_4 grains overlapped and cross-linked with each other.

(2) With the increased deposition time, the weight and density of porous Si_3N_4–Si_3N_4 composite ceramics increased and the porosity decreased. The weight increment was up to 162.27%. When the deposition time increased from 0 to 12 h, the density increased from 0.99 to 2.02 g/cm^3 and the porosity decreased from 68.65% to 26.07%. In addition, the dielectric constant increased from 1.72 to 3.60, with the dielectric loss remaining less than 0.01, indicating that porous Si_3N_4–Si_3N_4 composite ceramics possessed excellent EM wave-transparent performance. The flexural strength first improved with the deposition time, followed by a slight decrease. The maximum flexural strength of 47±2 MPa was attained at the deposition time of 6 h.

(3) After heat treatment, the porosity and dielectric constant of porous Si_3N_4–Si_3N_4 composite ceramics slightly increased and the flexural strength decreased. The porosity increased from 26.07% to 36.02%. The dielectric constant slightly increased from 3.60 to 3.70 with the dielectric loss remaining less than 0.01, exhibiting excellent EM wave-transparent ability of composite ceramics even at high temperature up to 1500 ℃. The flexural strength decreased from 35± 3.8 to 23.3±2.3 MPa due to the increased porosity and generation of micro-cracks.

Compared with Si_3N_4 ceramics via the traditional pressureless sintering process, the dielectric properties of porous Si_3N_4–Si_3N_4 composite ceramics via 3D printing combined with CVI technique were more adjustable, and the EM wave-transparent performance was remarkably improved. The present work provides a novel insight into the synthesis of Si_3N_4 ceramics with desired properties.

Acknowledgements

This work was supported by the Chinese National

Foundation for Natural Sciences under Contract (Nos. 51602258 and 51672217) and 111 Project of China (B08040).

References

[1] Li XM, Zhang LT, Yin XW. Fabrication and properties of porous Si_3N_4 ceramic with high porosity. *J Mater Sci Technol* 2012, **28**: 1151–1156.

[2] Ding SQ, Zeng YP, Jiang DL. Oxidation bonding of porous silicon nitride ceramics with high strength and low dielectric constant. *Mater Lett* 2007, **61**: 2277–2280.

[3] Wang HJ, Yu JL, Zhang J, *et al*. Preparation and properties of pressureless-sintered porous Si_3N_4. *J Mater Sci* 2010, **45**: 3671–3676.

[4] Wan T, Yao DX, Yin JW, *et al*. The microstructure and mechanical properties of porous silicon nitride ceramics prepared via novel aqueous gelcasting. *Int J Appl Ceram Technol* 2015, **12**: 932–938.

[5] Guo SQ, Hirosaki N, Yamamoto Y, *et al*. Hot-pressed silicon nitride ceramics with Lu_2O_3 additives: Elastic moduli and fracture toughness. *J Eur Ceram Soc* 2003, **23**: 537–545.

[6] Barta J, Manela M, Fischer R. Si_3N_4 and Si_2N_2O for high performance radomes. *Mater Sci Eng* 1985, **71**: 265–272.

[7] Yu JL, Wang HJ, Zeng H, *et al*. Effect of monomer content on physical properties of silicon nitride ceramic green body prepared by gelcasting. *Ceram Int* 2009, **35**: 1039–1044.

[8] Yin XW, Travitzky N, Greil P. Near-net-shape fabrication of Ti_3AlC_2-based composites. *Int J Appl Ceram Technol* 2007, **4**: 184–190.

[9] Seitz H, Rieder W, Irsen S, *et al*. Three-dimensional printing of porous ceramic scaffolds for bone tissue engineering. *J Biomed Mater Res* 2005, **74B**: 782–788.

[10] Zhao X, Evans JRG, Edirisinghe MJ, *et al*. Ceramic freeforming using an advanced multinozzle ink-jet printer. *J Mater Synth Proces* 2001, **9**: 319–327.

[11] Tay BY, Evans JRG, Edirisinghe MJ. Solid freeform fabrication of ceramics. *Int Mater Rev* 2003, **48**: 341–370.

[12] Blazdell PF, Evans JRG, Edirisinghe MJ, *et al*. The computer aided manufacture of ceramics using multilayer jet printing. *J Mater Sci Lett* 1995, **14**: 1562–1565.

[13] Song JH, Nur HM. Defects and prevention in ceramic components fabricated by inkjet printing. *J Mater Process Technol* 2004, **155–156**: 1286–1292.

[14] Li XM, Zhang LT, Yin XW. Effect of chemical vapor deposition of Si_3N_4, BN and B_4C coatings on the mechanical and dielectric properties of porous Si_3N_4 ceramic. *Scr Mater* 2012, **66**: 33–36.

[15] Naslain R. Design, preparation and properties of non-oxide CMCs for application in engines and nuclear reactors: An overview. *Compos Sci Technol* 2004, **64**: 155–170.

[16] Ma YZ, Yin XW, Fan XM, *et al*. Near-net-shape fabrication of Ti_3SiC_2-based ceramics by three-dimensional printing. *Int J Appl Ceram Technol* 2015, **12**: 71–80.

[17] Luo H, Tan YQ, Li Y, *et al*. Modeling for high-temperature dielectric behavior of multilayer C_f/Si_3N_4 composites in X-band. *J Eur Ceram Soc* 2017, **37**: 1961–1968.